Biosensors and Bioelectronics 123 (2019) 25–29

Contents lists available at ScienceDirect

Biosensors and Bioelectronics

journal homepage: www.elsevier.com/locate/bios

Co_3O_4 nanostructures on flexible carbon cloth for crystal plane effect of nonenzymatic electrocatalysis for glucose

Jianan Xu[a,c], Fenghua Li[a], Dandan Wang[a], Mian Hasnain Nawaz[a,d], Qingbo An[a], Dongxue Han[a,b], Li Niu[a,b,*]

[a] State Key Laboratory of Electroanalytical Chemistry, c/o Engineering Laboratory for Modern Analytical Techniques, Changchun Institute of Applied Chemistry, Chinese Academy of Sciences, Changchun 130022, PR China
[b] Center for Advanced Analytical Science, c/o School of Chemistry and Chemical Engineering, Guangzhou University, Guangzhou 510006, PR China
[c] University of Chinese Academy of Sciences, Beijing 100039, PR China
[d] Interdisciplinary Research Centre in Biomedical Materials (IRCBM), COMSATS University Islamabad, Lahore Campus, Pakistan

ARTICLE INFO

Keywords:
Crystal plane effect
Electrocatalysis
Nonenzymatic glucose sensor
Carbon cloth electrode
Co_3O_4

ABSTRACT

This work accounts the influence of facet effect of Co_3O_4 nanocrystals towards nonenzymatic electrocatalysis of glucose induced by different crystal planes modified on carbon cloth (CC) electrode. Tuning the molar ratio of precursor compounds during hydrothermal synthesis of Co_3O_4, followed by thermal decomposition protocols, different crystal structure including nanocubes, nanothorns, nanooctahedrons and nanosheets were obtained with respective {001}, {110}, {111} and {112} facets. The electrochemical results of these different Co_3O_4 crystals demonstrate that the nanooctahedron with crystal plane of {111} displays the best nonenzymatic electro-catalytic glucose activity with widest linear range (0.5–1000 μM), highest sensitivity (246.8 μA mM^{-1}) and detection limit of 0.012 μM (S/N = 3). Interestingly, the electrocatalytic activity for nonenzymatic electro-catalytic glucose is ranked in the order of {111} > {112} > {110} > {001}.

1. Introduction

Quantitative determination of glucose is important in various fields of research including food sciences (Holman et al., 2014; Shabnam et al., 2017), fuel cells (Bandodkar et al., 2016; Zhang et al., 2016), environmental and pharmaceutical industries (de Sales et al., 2018; Kirsch et al., 2013). In these lines, several methods have been applied for the quantitative detection of glucose. Electrochemical sensors, however, have been proved to be the industry standards for glucose sensing due to their low cost, rapid response, superior detection limits, and higher reliability (Dhara and Mahapatra, 2017; Kim et al., 2018; Xiao et al., 2017).

For last few decades, enzymatic glucose biosensors have dominated the glucose sensor industry. However, lack of chemical and thermal stability, operating temperature limitations, sensitivity towards humidity and pH, and the higher cost of the glucose oxidase prevent the enzymatic sensors in continuous monitoring applications. Alternatively, due to their unique properties, functionalized nanomaterials especially transitional metal based materials have extensively been used in many fields (Bing et al., 2017; Li et al., 2018; Shasha et al., 2017; Xu et al., 2017). Recently, several metal oxides such as ZnOx (Kong et al., 2009; Raza and Ahmad, 2018), MnOx (Han et al., 2017; Xiao et al., 2013), NiOx (Guo et al., 2018; Wang et al., 2012), CuOx (Chirizzi et al., 2016; Wang et al., 2010), CoOx (Ding et al., 2010; Kannan et al., 2017) have particularly been prepared as catalytic element for glucose sensors. Among these, CoOx has received much attention because of its excellent electro-catalytic properties and greater chemical stability. In recent years, many CoOx materials with different morphologies have been studied for glucose sensing (Kannan et al., 2017; Meng et al., 2016), but most of these studies were focused on the shape and morphology of sensing materials and no one detailed the effect of different crystal planes. Hence, there is great room to explore the crystal plane effect on the catalytic performance of CoOx.

In general, nanostructures with exposed high-energy crystal planes could display distinct and novel electrochemical properties, because crystal planes with much higher energies reduce the oxidation–reduction gaps, which ultimately could accelerate the reaction rates. Therefore, taking into account the anisotropic features and controlling the specific crystal planes the ion diffusion distance can rationally be reduce coupled with improved electronic conductivity. Recently, few

* Corresponding author at: State Key Laboratory of Electroanalytical Chemistry, c/o Engineering Laboratory for Modern Analytical Techniques, Changchun Institute of Applied Chemistry, Chinese Academy of Sciences, Changchun 130022, PR China.
E-mail addresses: dxhan@ciac.ac.cn (D. Han), lniu@ciac.jl.cn (L. Niu).

https://doi.org/10.1016/j.bios.2018.07.039
Received 28 April 2018; Received in revised form 12 July 2018; Accepted 17 July 2018
Available online 18 July 2018
0956-5663/

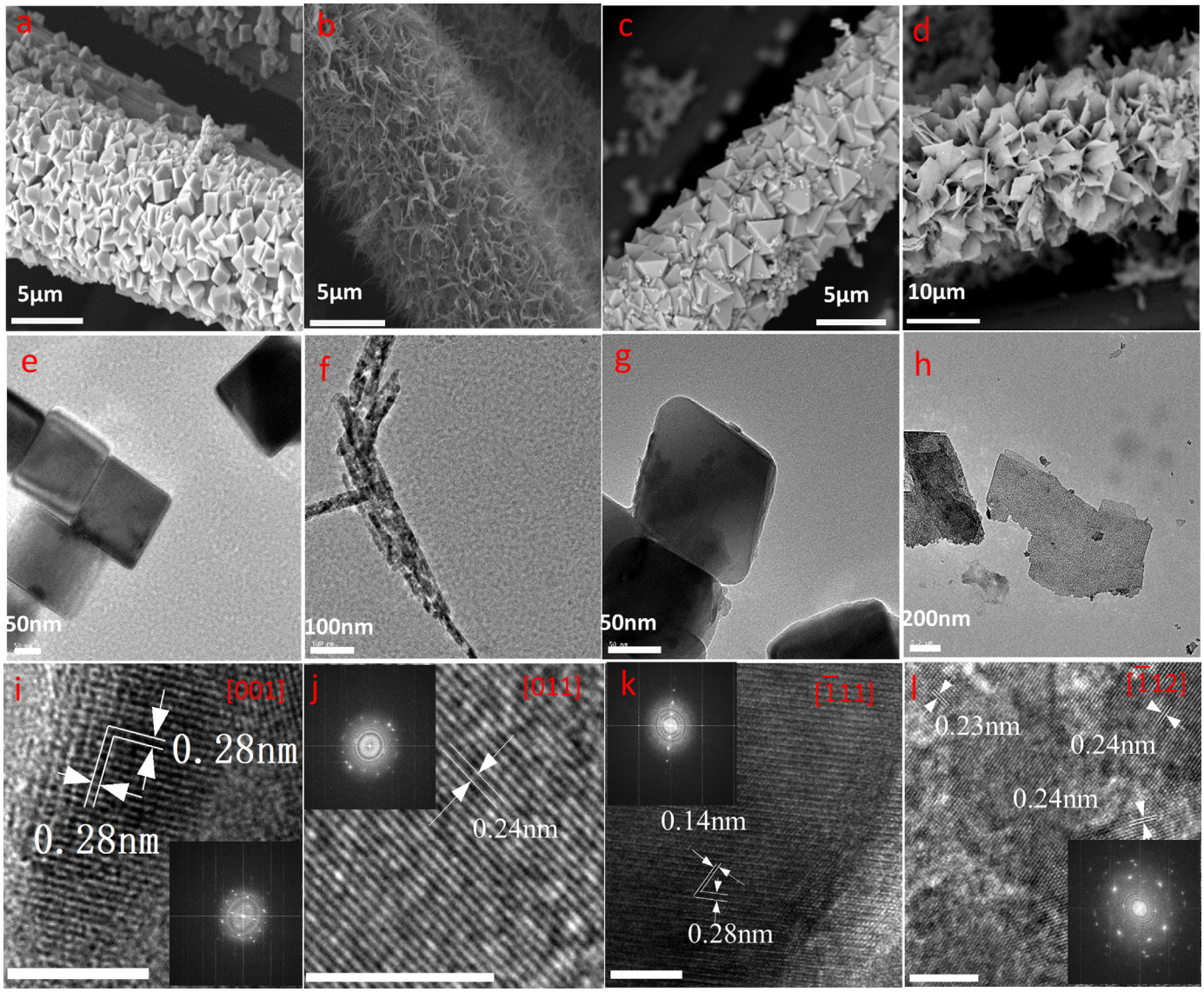

Fig. 1. (a–d) SEM, (e–h) TEM and (i-l) HRTEM images of different Co_3O_4 crystals directly grown on carbon cloth electrodes. (a, e, i) Co_3O_4 nanocubes, (b, f, g) Co_3O_4 nanothorns, (c, g, k) Co_3O_4 nanooctahedrons, and (d, h, l) Co_3O_4 nanosheets.

researchers documented the plane effects for electrochemical energy storage devices (Liu et al., 2013; Wang et al., 2017), supercapacitors (Wang et al., 2011), and electrocatalysis for overall water splitting (Liu et al., 2017). However, to best of our knowledge, little example of facet effect corroborated nonenzymatic glucose electrocatalysis has so far been reported. In this work, different crystal planes of Co_3O_4 including {001}, {110}, {111}, and {112} facets were grown on carbon cloth (CC) electrode. Corresponding to the Co_3O_4 different morphology of {001}, {110}, {112} and {111} crystal plane the respective electrodes were termed as nanocube electrode (NCE), nanothorn electrode (NTE), nanosheet electrode (NSE) and nanooctahedron electrode (NOE). The electrochemical responses towards glucose electrocatalysis demonstrate that the prepared electrodes display high performances, especially NOE, which shows a widest linear range and lowest detection limit.

2. Results and discussions

Prior to modification electrodes were cleaned by sonication, followed by Co_3O_4 nanocrystal growth bearing different crystal planes. Different crystal morphologies were obtained by changing the molar ratio of precursor compounds via hydrothermal method, as illustrated in Fig. S1. After hydrothermal decomposition the modified electrodes were performed structural and electrochemical characterizations. More experimental details can be envisioned in Supporting information.

Scanning electron microscopy (SEM) images of Co_3O_4 with different morphologies were shown in Fig. 1a–d to demonstrate the uniformity and regularity in ultimate products. It is clear that the products on CC were uniform with regular shapes. In addition, sheet-like and thorn-like nanostructures were vertically grown on the surface of CC. (Fig. 1b and d). High-magnification SEM images were shown in Fig. S2. The insight into the morphologies were further fancied by transmittance electronic microscopy (TEM) and high-resolution transmittance electron microscopy (HRTEM), Fig. 1i–l and corresponding fast Fourier transform (FFT) patterns (inset). As shown in Fig. 1e, cube-like Co_3O_4 with average size of 200 nm showing smooth surfaces, perfect sharp edges and corners and well-defined faces. Similarly, well ordered and uniform morphology of thorn-like and sheet-like Co_3O_4 can be envisioned in Fig. 1f–h, respectively. Moreover, octahedron-like architectures of 100 nm size with smooth surfaces and mild edges. Fig. 1i–l were observed by HRTEM analysis. In the HRTEM image of the cube-like Co_3O_4 (Fig. 1i), two sets of crystal planes (0.28 nm) were revealed along with two mutually perpendicular orientations, which are fixed to [$\bar{2}$20] and

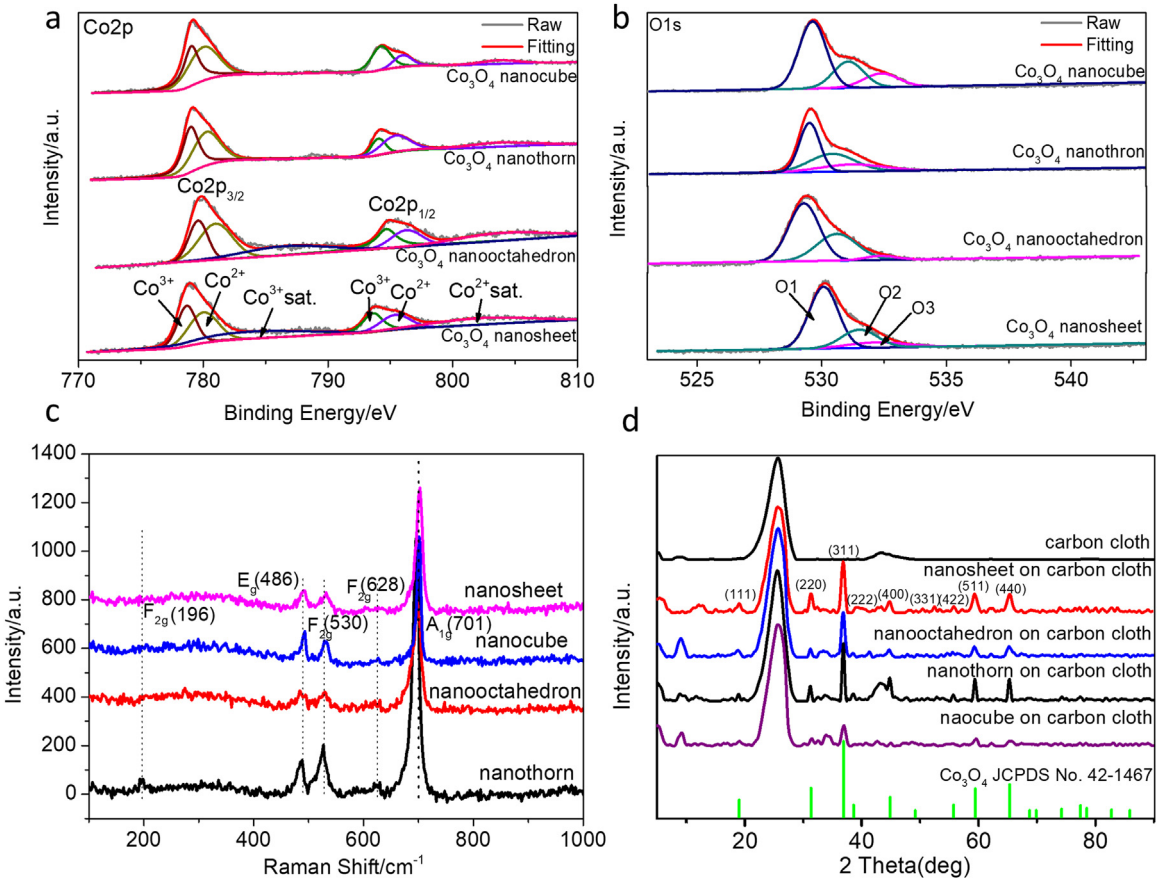

Fig. 2. (a) Co 2p and (b) O 1s XPS spectra, (c) Raman patterns and (d) XRD patterns for the Co_3O_4 nanocube, nanothorn, nanooctahedron, and nanosheet structures on carbon cloth electrodes.

[220]. According to structural analysis, the normal direction to the entirely exposed crystal plane is indexed as [001], indicating the exposure of {001} crystal plane group. Likewise, crystallization orientation of [31$\bar{1}$] was shown in Fig. 1j, indicated the [011] crystal orientation in accordance with the FFT pattern (inset), corresponding to {110} crystal plane group. Fig. 1k displayed the crystal lattice spacing of 0.14 nm and 0.28 nm with an included angle of 60°, corresponding to the crystal orientation of [101] and [220], which corresponds to the crystal plane group of {111}. The [$\bar{1}$12] zone axis was shown in Fig. 1l with the crystal orientation of [$\bar{1}$1$\bar{1}$] and [311], bearing the crystal lattice spacing of 0.23 nm and 0.24 nm and the crystal orientation demonstrated the {112} crystal plane group.

The X-ray photoelectron spectroscopy (XPS) spectra of Co 2p and O 1s were shown in Fig. 2a–b. In case of Co 2p spectra all four samples revealed two distinct peaks correspond to Co $2p_{1/2}$ and Co $2p_{3/2}$ (Schenck et al., 1983; Wang et al., 2014) at binding energies of 779.8 and 795.2 eV accompanying with two weaker satellite peaks separated by 15.4 eV (spin–energy separation), as shown in Fig. 2a. Furthermore, the principle peaks cold be fitted into four subpeaks, of which the fitting peaks at 781.0 and 796.3 eV with the satellite peak at 786.6 eV were indexed to Co(II), and peaks at 779.6 and 794.7 eV with the satellite peak at 804.0 eV correspond to Co(III) (Marco et al., 2000). Moreover, the largest proportion of Co^{3+} was revealed in Co_3O_4 octahedron nanostructure, demonstrating the highest catalytic activity of {111} crystal plane. Likewise, the fitting peaks signed as O 1 and O 2 with binding energies of 529.63 and 531.06 eV correspond to the lattice oxygen of Co_3O_4 crystals and the OH species absorbed onto the surface of the obtained nanostructures (Xiong et al., 2012). It is worth mentioning that O 3 with binding energies of 532.38 eV correspond to multiplicity of physically absorbed and chemisorbed species (Marco et al., 2000) gradually decreased from Co_3O_4 cube nanostructure to octahedron nanostructure.

Similarly, Raman spectra (Fig. 2c) revealed that the features in low-wavenumber region match well with the prominent characteristic Raman active modes of Co_3O_4, in which the peaks located at 196, 530, and 628 cm^{-1} are indexed to the F_{2g} mode of Co_3O_4, and the peaks at 486 and 701 cm^{-1} are attributed to E_g and A_{1g} modes, respectively (Hadjiev et al., 1988). Likewise, the powder X-ray diffraction (XRD) patterns of four morphologies found indexed to the standard JCPDS card 42–1647 of Co_3O_4, as revealed in Fig. 2d. Additionally, some characteristic peaks corresponding to crystalline carbon were also found in the XRD patterns which signalled the presence of CC substrate, used for the growth of Co_3O_4. Energy dispersive spectrometry (EDS, Fig. S4) and EDS mapping (Fig. S5) further confirmed the co-existence of three elements (C, Co, O) in all the samples. The abundance of C was due to the CC substrate while the atomic ratio of Co and O was found to be about 3:4 which corroborated the successful synthesis of CC-supported Co_3O_4.

Electrochemical impedance spectroscopy (EIS) was carried out to explore electrochemical kinetics of different Co_3O_4 crystal facets towards glucose electrocatalysis. Fig. 3a exhibiting the impedance spectra of all the four crystal structures of Co_3O_4 and the inset showing corresponding circuit model fitting. The semicircles in the high frequencies indicated the bulk membrane resistance followed by an interfacial charge-transfer process in the region of low frequencies. The circuit model consists of in series resistance (R_S) and a parallel branch involving an interfacial constant phase element (CPE) and charge-transfer resistance (R_{ct}) with Warburg impedance (Z_w). NOE owns a much lower R_{ct} value of 30.95 Ω than that of NCE (839.5 Ω), NTE (653 Ω) and NSE (160.2 Ω). Impedance at the interface between the electrode and

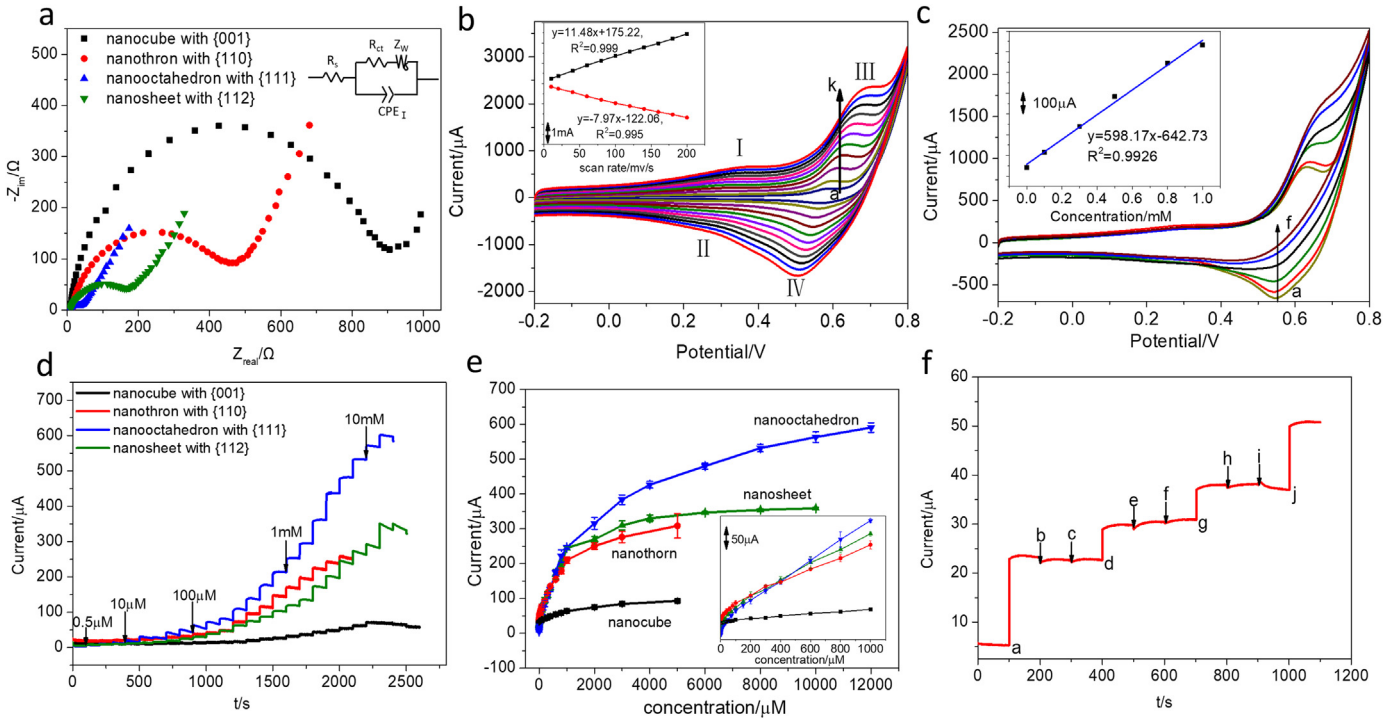

Fig. 3. (a) Nyquist plots and the equivalent circuit (inset) of {001}, {110}, {111} and {112} crystal planes. CVs of NOE in 0.1 M NaOH solution (b) with different scan rates, (c) at various concentrations of glucose: 0, 0.1, 0.3, 0.5, 0.8 and 1 mM with the scan rate of 60 mV/s. Inset (b) is the plot of peak currents *vs*. scan rate and inset (c) is plot of the oxidation currents *vs*. concentration of glucose (d) Typical amperometric response of CC electrodes modified with Co_3O_4 nanocube (at 0.35 V), nanothorn (at 0.43 V), nanooctahedron (at 0.54 V) and nanosheet (at 0.40 V) against successive addition of glucose in 0.1 M NaOH. (e) Corresponding calibration curve vs. glucose concentration. Inset (e) is a zoom of linear range. (f) Amperometric response of NOE at 0.54 V towards the addition of 10 μM glucose (steps a, d, g and j) and interfering compounds of 1 μM sucrose (b), fructose(c), lactose(e), LA (f), UA(h), and AA(i) in 0.1 M NaOH solution.

aqueous phase can be described by the charge-transfer resistance (R_{ct}), which eventually reflects the easiness of the electron-ion transfer processes. Therefore, bearing such lower value of R_{ct} the {111} crystal plane involves in faster charge transport which consequently fortifies the electrochemical oxidation of glucose.

Cyclic Voltammetry profiles (CVs) with different scan rates of NOE were tested in 0.1 M NaOH as shown in Fig. 3b. Two pairs of redox peaks were observed, resulting from the reversible transition between Co_3O_4 and CoOOH (I/II) and the transition between CoOOH and CoO_2 (III/IV) (Kannan et al., 2017), which was due to the participation of OH^- in the electrochemical redox reaction of Co_3O_4. Besides, the redox peak currents and peak to peak separation (ΔEp) increase linearly with the increasing scan rates (10 mv/s to 200 mv/s, inset in Fig. 3b). As shown in Fig. 3c, the oxidation and reduction peak current (III) and (IV) increased significantly upon increasing the concentration of glucose. Additionally, the corresponding calibration curve (inset in Fig. 3c) displays a linear correlation over a concentration range from 0.1 mM to 1 mM of glucose with a correlation coefficient of 0.9926, indicating the excellent applicability of the flexible NOE. As a comparison all the crystals facets were also analyzed for different scan rates and with increasing glucose concentrations and experiments intimated the better electrochemical performances in case of NOE, as shown in Figs. S6 and S7.

Different potentials (corresponding to peak III and IV) were applied for the non-enzymatic amperometric detection of glucose to all the four electrodes in 0.1 M NaOH solution, as shown in Fig. S8. These amperometric responses suggested the superior stability and sensitivity of NOE at potential of 0.54 V. Likewise, for comparison of all the Co_3O_4 modified electrodes amperometric responses were studied at their corresponding reduction potentials e.g. nanocube (at 0.35 V), nanothorn (at 0.43 V), and nanosheet (at 0.40 V), as shown in Fig. 3d. Four distinct current-time (i-t) curves with sharper increase in the amperometric response on successful injection of glucose were obtained, even with glucose concentrations as low as 0.5 μM (Fig. 3d). A wide linear range response of glucose with NOE was obtained (0.5 μM to 1 mM) superior to the other electrodes (0.5 μM-0.4 mM, Fig. 3e). The error bar in Fig. 3e shows the different amperometric responses at the same operational conditions between five parallel electrodes. It depicts that the prepared electrodes display good reproducibility. The sensitivity (64.71 $\mu A\,cm^{-2}\,mM^{-1}$) and limit of detection (0.012 μM, S/N = 3) of NOE were calculated from Fig. 3e using standard deviation of the baseline current (Zare et al., 2005) and the values were found superior to the others as shown in Table S2.

The selectivity of NOE was investigated against several biomolecules including lactic acid (LA), uric acid (UA), ascorbic acid (AA), sucrose, lactose and fructose, which might coexist with glucose. As shown in Fig. 3f, it is clear that the addition of another carbohydrate had little influence on glucose electrochemical signals with NOE. Compared to previously reported typical non-enzymatic glucose sensor based on Co_3O_4 (Table S3), NOE exhibits superior sensitivity and detection limit towards glucose.

Furthermore, the reproducibility of the Co_3O_4 modified on CC glucose sensor was evaluated at a given concentration of glucose (10 μM) for five successive measurements. As shown in Fig. S9, it is clear that NOE maintains at least 86% of the initial value after 21 days, suggesting it has great long-term stability and reproducibility.

3. Conclusions

In brief, Co_3O_4 with different morphologies (nanooctahedrons, nanocubes, nanothorns and nanosheets) and varying crystal planes were successfully synthesized onto CC electrode and were used as nonenzymatic electro-catalysts for glucose oxidation. In particular, the Co_3O_4 nanooctahedron with {111} facet displayed best electro-catalytic glucose activity compared with other Co_3O_4 architectures. Since the Co_3O_4 nanooctahedron with {111} facet modified CC electrode possess

the largest electrochemically active surface area, the highest catalytic activity, and the fastest electron-ion transfer process, it exhibited superior catalytic activity towards the electrochemical oxidation of glucose. The nonenzymatic electro-catalytic glucose activity decreased as the crystal plane of Co_3O_4 nanocrystals changed from {111} to {001}. This work demonstrates the potential of crystal plane induced activity of Co_3O_4 nanocrystals in non-enzymatic electrochemical glucose sensors with meliorated electrochemical performances and device fabrication protocols.

Acknowledgements

This work was supported by NSFC, China (21622509, 21527806, and 21475122), the Department of Science and Techniques of Jilin Province (2160201008GX, 20170203004SF and 20170101183JC) and Jilin Province Development and Reform Commission (2016C014 and 2017C053-1), Science and Technology Bureau of Changchun (15SS05).

Appendix A. Supporting information

Supplementary data associated with this article can be found in the online version at doi:10.1016/j.bios.2018.07.039.

References

Bandodkar, A.J., Jeerapan, I., You, J.M., Nunez-Flores, R., Wang, J., 2016. Nano Lett. 16 (1), 721–727.
Bing, L., Peng, G., Yongcheng, F., Guangxun, Z., Kesheng, H., Huaiguo, X., Huan, P., 2017. Adv. Funct. Mater. 27 (12), 1605784.
Chirizzi, D., Guascito, M.R., Filippo, E., Malitesta, C., Tepore, A., 2016. Talanta 147, 124–131.
de Sales, N.F.F., Silva da Costa, L., Carneiro, T.I.A., Minuzzo, D.A., Oliveira, F.L., Cabral, L.M.C., Torres, A.G., El-Bacha, T., 2018. Molecules 23 (3).
Dhara, K., Mahapatra, D.R., 2017. Microchim. Acta 185 (1), 49.
Ding, Y., Wang, Y., Su, L., Bellagamba, M., Zhang, H., Lei, Y., 2010. Biosens. Bioelectron. 26 (2), 542–548.
Guo, X., Zhang, G., Li, Q., Xue, H., Pang, H., 2018. Energy Storage Mater. 15, 171–201.
Hadjiev, V.G., Iliev, M.N., Vergilov, I.V., 1988. J. Phys. C 21 (7), L199.
Han, L., Shi, J., Liu, A., 2017. Sens. Actuators B 252, 919–926.
Holman, R.R., Sourij, H., Califf, R.M., 2014. Lancet 383 (9933), 2008–2017.
Kannan, P., Maiyalagan, T., Marsili, E., Ghosh, S., Guo, L., Huang, Y., Rather, J.A., Thiruppathi, D., Niedziolka-Jonsson, J., Jonsson-Niedziolka, M., 2017. Analyst 142 (22), 4299–4307.
Kim, J., Campbell, A.S., Wang, J., 2018. Talanta 177 (Suppl. C), S163–S170.
Kirsch, J., Siltanen, C., Zhou, Q., Revzin, A., Simonian, A., 2013. Chem. Soc. Rev. 42 (22), 8733–8768.
Kong, T., Chen, Y., Ye, Y., Zhang, K., Wang, Z., Wang, X., 2009. Sens. Actuators B 138 (1), 344–350.
Li, X.R., Wei, J.L., Li, Q., Zheng, S.S., Xu, Y.X., Du, P., Chen, C.Y., Zhao, J.Y., Xue, H.G., Xu, Q., Pang, H., 2018. Adv. Funct. Mater. 28 (23).
Liu, L., Jiang, Z., Fang, L., Xu, H., Zhang, H., Gu, X., Wang, Y., 2017. ACS Appl. Mater. Interfaces 9 (33), 27736–27744.
Liu, D., Wang, X., Wang, X., Tian, W., Bando, Y., Golberg, D., 2013. Sci. Rep. 3.
Marco, J.F., Gancedo, J.R., Gracia, M., Gautier, J.L., Ríos, E., Berry, F.J., 2000. J. Solid State Chem. 153 (1), 74–81.
Meng, S.J., Wu, M.Y., Wang, Q., Dai, Z.Y., Si, W.L., Huang, W., Dong, X.C., 2016. Nanotechnology 27 (34), 7.
Raza, W., Ahmad, K., 2018. Mater. Lett. 212, 231–234.
Schenck, C.V., Dillard, J.G., Murray, J.W., 1983. J. Colloid Interface Sci. 95 (2), 398–409.
Shabnam, L., Faisal, S.N., Roy, A.K., Haque, E., Minett, A.I., Gomes, V.G., 2017. Food Chem. 221, 751–759.
Shasha, Z., Xinran, L., Bingyi, Y., Qin, H., Yuxia, X., Xiao, X., Huaiguo, X., Huan, P., 2017. Adv. Energy Mater. 7 (18), 1602733.
Wang, X., Hui, C., Liu, H., Du, G., He, X., Xi, Y., 2010. Sens. Actuators B 144 (1), 220–225.
Wang, Y., Lei, Y., Li, J., Gu, L., Yuan, H., Xiao, D., 2014. ACS Appl. Mater. Interfaces 6 (9), 6739–6747.
Wang, G., Lu, X., Zhai, T., Ling, Y., Wang, H., Tong, Y., Li, Y., 2012. Nanoscale 4 (10), 3123–3127.
Wang, H., Wang, L., Chen, S., Li, G., Quan, J., Xu, E., Song, L., Jiang, Y., 2017. J. Mater. Chem. A 5 (7), 3569–3577.
Wang, Y., Zhong, Z., Chen, Y., Ng, C.T., Lin, J., 2011. Nano Res. 4 (7), 695.
Xiao, F., Li, Y., Gao, H., Ge, S., Duan, H., 2013. Biosens. Bioelectron. 41, 417–423.
Xiao, X., Zheng, S., Li, X., Zhang, G., Guo, X., Xue, H., Pang, H., 2017. J. Mater. Chem. B 5 (26), 5234–5239.
Xiong, S., Chen, J.S., Lou, X.W., Zeng, H.C., 2012. Adv. Funct. Mater. 22 (4), 861–871.
Xu, Y., Zheng, S., Tang, H., Guo, X., Xue, H., Pang, H., 2017. Energy Storage Mater. 9, 11–30.
Zare, H.R., Memarzadeh, F., Ardakani, M.M., Namazian, M., Golabi, S.M., 2005. Electrochim. Acta 50 (16), 3495–3502.
Zhang, E., Xie, Y., Ci, S., Jia, J., Wen, Z., 2016. Biosens. Bioelectron. 81 (Suppl. C), S46–S53.